HIGH CURRENT TRAVELING WAVE ELECTRON LINEAR ACCELERATORS

J. Haimson

Varian Associates
Palo Alto, Calif.

Summary

The steady state and stored energy operational regimes of microwave electron linear accelerators are discussed with reference to high current capability. Avoidance of the beam blow-up pulse shortening phenomenon enables long pulse beam currents considerably greater than the maximum conversion efficiency value to be demonstrated. Heavy beam loading effects and choice of frequency are discussed with respect to this steady state operation, and it is shown that conversion efficiencies of greater than 90 per cent can be readily achieved. Stored energy considerations indicate that an increase in peak current of one or two orders of magnitude may be achieved for pulses of short duration with relatively conventional accelerator waveguides. Electron orbit theory including space charge effects for this transient condition is developed. Some experimental data obtained with a 10 Mev linear accelerator using a short pulse inflection system is presented. A concluding discussion deals with design criteria for stored energy operation in high power traveling wave structures and encourages further exploitation by providing higher current high potential sources capable of prebuncher or r-f chopped short pulse injection.

Introduction

The microwave linear accelerator provides an efficient and practical means of imparting energy to an electron beam by extended interaction in a traveling electric field environment, the propagation parameters of which may be selected to satisfy a wide variety of beam specifications.

Early applications concentrated on the attainment of electron beams of high energy but of modest intensity, rarely exceeding several hundred milliamperes of peak current. These accelerators operating within the restrictions of the available microwave sources provided beam pulse lengths of several microseconds duration at repetition rates of up to several hundred pulses per second. In recent years growing interest in such fields as pulse radiolysis, pulse radiography, plasma physics, neutron time-of-flight, nuclear weapon radiation simulation, super power short pulse r-f generation, etc., established a requirement for, and encouraged investigations into the attainment of, higher peak currents at megavoltage energies.

The following discussion has been separated into two catagories (a) the steady state mode of operation in which equilibrium conditions have been established between the applied and beam induced r-f fields along the full length of the waveguide, and (b) the stored energy regime in which a fast rise beam pulse is switched into a fully excited microwave circuit to extract stored energy under the transient conditions that exist when the beam pulse is shorter than the r-f fill time. This latter category offers more opportunity to demonstrate high current pulses and will be considered at greater length in the following discussion than the steady state case.

Steady State Operation

The general theory of electron linear accelerator operation under steady state conditions has been adequately covered in the literature and a selection of representative papers has been included in the bibliography.[1-7] It has been shown[5] that for accelerator waveguides of uniform impedance the maximum conversion efficiency (η_m) of r-f to beam power is related to the total circuit voltage attenuation (IL) in nepers by

$$\eta_m = \left(\frac{i_m V_m}{P_o}\right) = \frac{1}{2}\,\frac{\left(1 - e^{-IL}\right)^2}{IL - \left(1 - e^{-IL}\right)} \qquad (1.1)$$

and the beam loading characteristics of a waveguide is such that the maximum conversion efficiency is realized at that value of peak current (i_m) which reduces the unloaded beam energy to half value. For given levels of input power, lower attenuation circuits are favored for the attainment of higher conversion efficiencies and beam currents. It is indicated that steady state (long pulse) operation of up to several amperes of peak current should be possible at L or S band frequencies with nominal r-f power levels in the 10-20 MW range. Experience recounts, however, that electron linear accelerators of early design failed to demonstrate maximum conversion efficiency owing to pulse current limitations imposed by the phenomenon of beam blow-up.[8-11] This effect caused a rapid decrease of the pulse length of the emergent electron beam if attempts were made to increase the current above a critical value (i_s). Reported values of i_s ranged from approximately 150 to 850 ma for accelerators of differing design operating with beam pulse lengths in the range of one to five microseconds, and in most cases these critical currents were only 60 to 90 per cent of the i_m value. Investigation of the pulse shortening phenomenon established that a higher order mode was excited by the beam and that a regenerative feed back mechanism, similar to a backward wave oscillator, enabled sufficient power to be coupled into this mode for the beam to become radially deflected and lost to the inner surfaces of the waveguide. It appears that a hybrid type TM_{11} mode with non-compensating deflections due to the transverse magnetic and radial electric field components is responsible, and the (i_s) values of critical starting current for a given pulse length are

strongly dependent upon such factors as the high order mode group velocity, the slip parameter which depends upon the velocity difference between the wave and the particle and the length of the circuit. Most of the techniques used to prevent or attenuate this interaction have in common the design of non-uniform impedance waveguide structures which prevent growth of the higher order fields without unduly affecting the fundamental accelerating axial electric field. There appears good reason to believe however, that for very high currents and extended pulse lengths it may be necessary to adopt differential absorption techniques for these higher modes within individual cavities especially when operating in high interaction impedance regions close to the edge of the pass band.

More recently, design values of high current and maximum conversion efficiency have been demonstrated under long pulse operating conditions with variable impedance waveguides. Some typical performance information is compared against earlier uniform impedance designs in Table I. It should be noted that the use of $2\pi/3$ mode uniform waveguide does not necessarily prevent pulse shortening. In fact, a high interaction impedance in the vicinity of $a/\lambda=0.19$ can result in relatively low values of starting oscillation current especially for long circuits. Over the typical S-band $2\pi/3$ impedance working range this hybrid mode has a pass band range of 50-250 Mc.

Prevention of the pulse shortening phenomenon can now lead to maximum exploitation of lower attenuation waveguides operating at high peak power to achieve limiting values of i_m. For example, the i_m upper limits for constant gradient $2\pi/3$ waveguides for different power levels at S and L-band frequencies and over a range of low attenuation parameters are shown in Figure 1. This indicates that steady state operation with maximum i_m values of four to five amperes and conversion efficiencies of 90 to 95 per cent can be demonstrated with presently available r-f generators. These η_m values will be reduced for the first accelerator section because of the energy loss during bunching.

The problem of bunching large containments of charge will be discussed in a later section but in general, this requires phase positioning ahead of the crest of the r-f wave. Energy spectra broadening due to heavy beam loading can be reduced by minimizing the debunching effect of space charge fields, especially during the initial wave lengths of the trajectory, and counteracting excessive reactive phase shifts,[12] by non-synchronous or section phase-staggered operation. It is also desirable at higher current levels, say greater than one or two amperes, to provide good prebunching at injection into the accelerator to avoid unnecessary loading and charge build up due to unaccepted electrons which fall outside of the accelerating electric field binding region.

Stored Energy Operation

On the basis that the stored energy per unit length (u_z) at a point z within a traveling wave microwave circuit may be written

$$u_z = P_z/v_{gz} \tag{2.1}$$

where P_z is the energy flux and v_{gz} the group velocity at z, the total stored energy (U) may be written

$$U = \int_0^L P_{z/v_{gz}}\, dz = P_o T_f F(IL) \tag{2.2}$$

where P_o is the input power, T_f the fill time and F(IL) an attenuation factor which for most cases $0.5 < F(IL) < 1.0$. With a 20 megawatt r-f source and fill times of the order of a microsecond, 10 to 20 joules can be readily stored in a waveguide at nominal field strengths to give approximately 10 Mev. On the basis of 50% energy extraction, therefore, a simple consideration neglecting the initial bunching problem indicates that levels of pulse charge of up to 1000 ampere nanoseconds (Ans) can be achieved providing that the pulse lengths are short compared to the r-f fill time. In order to more accurately analyze this beam switching mechanism the transient power flow characteristics of the circuit have to be established and the inherent capability of accelerating very large currents requires a more detailed investigation of the space charge electric fields especially during the critical early bunching stages. A knowledge of the circuit electric field pattern in time and space suitably modified by the space charge fields as a function of the changing bunch geometry and for a given charge content enables (a) the initial bunching characteristics to be studied (b) the overall energy gain at any time during the pulse to be computed and (c) the energy spectra to be obtained from (a) and (b) as well as the total energy transferred to the beam.

Transient Electric Field and Electron Energy Gain

The following discussion will in general be confined to microwave circuits that have been filled prior to injection of a short uninterrupted beam pulse. If the injected beam pulse (T_b) is short compared to the fill time (T_f), r-f equilibrium conditions will be established only over a short initial portion of the circuit the length of which will depend upon the time interval after commencement of the beam pulse and the group velocity characteristics within this portion of the circuit. A transient condition will exist throughout the remainder of the accelerator waveguide such that each of the cavities contained therein will transfer a portion of the energy stored in the r-f fields to successive bunches of electrons. This time and current dependent depletion of the total electric field will result in less energy gain for subsequent bunches causing an inherent broadening of the energy spectra. The resultant longitudinal electric field in space and time (E_{zt}) may be obtained by considering superposition of the beam induced field ($E_{bz,t}$) and the synchronous Fourier component of the impressed field (E_{oz}). Therefore, a knowledge of the growth of the beam induced component in time and space together with the particle phase position will enable beam energy (V_{zt}) to be obtained.

With the understanding that the waveguide group velocity (v_g) is defined as the ratio of energy flux to the energy density per unit length and has the usual definition,

$$v_g = \omega/2IQ \qquad (2.3)$$

where I is the voltage attenuation per unit length, the group velocity will determine the rate at which an energy disturbance can propogate along the circuit. In considering variable impedance waveguides v_g will be a function of z and consequently the distance traveled in a time interval Δt will be

$$\Delta z = \bar{v}_{gz}\Delta t, \qquad (2.4)$$

where $\bar{v}_{gz}$ is the effective mean value of v_{gz} over the distance Δz, and the total fill time can be expressed as,

$$T_f = \int_0^L \frac{dz}{v_{gz}} \qquad (2.5)$$

Immediately after transit of the initial portion of the pulse, electic fields will be induced within each cavity ($\Delta E_{bz} = irI\Delta z$) giving rise to a "beam loading" disturbance which will commence propagation simultaneously (assume $\beta_e >> v_{gz}/c$) from all the cavities in accordance with their individual group velocity characteristics. Providing the beam pulse remains uninterrupted, a distance equal to $\bar{v}_{gz}t$ will be transversed from any given point after a time interval t. It is clear that a growth pattern will develop from the beginning of the guide and the distance $z = \bar{v}_{gz}t$ will represent a region over which steady state conditions have been established. i.e., the energy flow out of this region is in equilibrium with that supplied by the uninterrupted traversal of subsequent electron bunches. A simple representation of this induced field growth mechanism (distance and time) is shown in Fig. 2A. The waveguide has been divided up into arbitrary lengths and although it is not intended that the horizontal field profile be representative of any particular circuit it will be seen later that transient electric fields can be produced having constant amplitude along the waveguide. The broken line oz represents the increasing steady state amplitude of the induced field as the point z progresses along the guide with time. It can also be seen however, that energy arriving at any point z_n in the "transient" section $z<z_n<L$, has a corresponding starting position z_{on} at time t=o, i.e., in the absence of the electron beam. By considering z_n fixed, it can be seen that the point z_{on} travels back toward the start of the circuit such that

$$z_{on} = z_n - \bar{v}_{gzn}t \qquad (2.6)$$

The already established impressed field, due to the power flow conditions existing at t=o i=o, will be opposed by the induced fields during particle acceleration. The resultant field condition at z_n can therefore be determined with respect to z_{on} in a similar manner to the steady state field at z in respect to the beginning of the guide by allowing for the power difference between z=o and z_{on} at time t=o, i.e., copper losses only. (If the guide is not filled prior to beam injection then the impressed field will also be time dependent (E_{ozt}) but the power modification at z_{on} will still be for conditions existing at t=o the start of the beam pulse.)

Constant Gradient Circuit

In designing a variable impedance waveguide for constant gradient, say, in the absence of the electron beam, it is required that the electric field $E_{oz}=(2I_z r_z P_z)^{1/2}$ remain constant for any value of z. This in turn requires that $2I_z P_z$, the copper loss per unit length, remains constant for any z. By disregarding the slight increase in shunt impedance (r), due to the reduction in disc aperture as I is increased to compensate for power attenuation, this results in a linear power decay accompanied by an inverse linear function of I. By also disregarding the slight decrease in Q with aperture dimension, equation (2.3) indicates that the group velocity will decrease linearly along the guide.

It has been shown[6] that the steady state r-f power flow (P_z) under these conditions is given by

$$\left(P_z/P_o - Y_o z\right)^{1/2} = 1 - i/2\left(r/Y_o\right)^{1/2}\ln\left(P_o/P_o - Y_o z\right) \qquad (2.7)$$

where Y_o is the average power loss per unit length of the waveguide, P_o is the input power, i the peak current and the attenuation per unit length varies as

$$I_z = Y_o/2\left(P_o - Y_o z\right) \qquad (2.8)$$

Substitution of equations (2.7) and (2.8) into $E_z=(2I_z r P_z)^{1/2}$ gives the steady state total electric field expression

$$E_z = \left(Y_o r\right)^{1/2}\left[1 - \frac{i}{2}\left(\frac{r}{Y_o}\right)^{1/2}\ln\left(\frac{P_o}{P_o - Y_o z}\right)\right] \qquad (2.9)$$

Referring again to Fig. 2A, over the steady state region $o < z \le \bar{v}_{gz}t$, the electric field will be represented by equation (2.9) and for the transient region $\bar{v}_{gz}t < z_n < L$ we can modify the power equation (2.7) by replacing P_o with $P_{on}(= P_o - Y_o z_{on})$ giving,

$$\left[\frac{P_{znt}}{(P_o - Y_o z_{on}) - Y_o(z_o - z_{on})}\right]^{1/2} = 1 - \frac{i}{2}\left(\frac{r}{Y_{on}}\right)^{1/2}\ln\left(\frac{P_o - Y_o z_{on}}{P_o - Y_o z_{on} - Y_{on}\left[z_n - z_{on}\right]}\right) \qquad (2.10)$$

Because of the constancy of the average power loss per unit length $Y_o = Y_z = Y_{on}$, and substituting for I_{zn} in $E_{znt}=(2I_{zn}rP_{zn})^{1/2}$ we obtain

$$E_{znt} = \left(Y_o r\right)^{1/2}\left[1 - \frac{i}{2}\left(\frac{r}{Y_o}\right)^{1/2}\ln\left(\frac{P_o - Y_o z_{on}}{P_o - Y_o z_n}\right)\right] \qquad (2.11)$$

However, z_{on} is time and distance dependent upon z_n because of the changing group velocity along the circuit and by substituting (2.8) in (2.3) and integrating (2.5) from z_{on} to z_n we obtain

$$\left(P_o - Y_o z_{on}\right)/\left(P_o - Y_o z_n\right) = e^{\omega t/Q} \qquad (2.12)$$

to give

$$E_{znt} = \left(Y_o r\right)^{1/2}\left[1 - \frac{i}{2}\left(\frac{r}{Y_o}\right)^{1/2} e^{\omega t/Q}\right] \qquad (2.13)$$

the constant amplitude value of the resultant field

at t over the transient region $\bar{v}_{gz} t < z_n < L$.

Figure 2B shows the steady state and transient induced fields combined with the impressed field (E_{oz}) for a fixed peak current and two values of t. The broken curves represent corresponding transient fields in a uniform impedance waveguide of the same IL and for the same input power and beam loading conditions. For equal pulse times, the advanced position of Q' with respect to Q, due to the higher initial group velocity, combined with the enhanced terminal field strengths of the constant gradient design results in a lower energy spread during the pulse.

The total energy gain can be obtained as a function of time during the pulse by integrating (2.9) from zero to z and (2.13) from z to L. Then by substituting

$$z = \frac{P_o}{Y_o}\left(1 - e^{-\omega t/Q}\right)$$

as obtained from equations (2.8), (2.3) and (2.5) and $T_f = 2IL\,Q/\omega$, the voltage can be expressed in terms of fill time and attenuation by

$$V_t = \sqrt{rLP_o\left(1-e^{-2IL}\right)} - \frac{irL}{2\left(1-e^{-2IL}\right)}\left[1-2IL\,\frac{t}{T_f}e^{-2IL} - e^{-2IL\,t/T_f}\right] \qquad (2.14)$$

In general, the injected current density varies with time during high current short pulse operation and under these circumstances

$$i = 1/t\int_o^t i_t\,dt$$

should be inserted in the above equations. Figure 2B shows the s-shaped modification caused by a triangular pulse distribution of the same total charge and duration ($0.2T_f$) as the uniform pulse which produced the sloping field pattern PQR.

The total extracted energy during the beam pulse (T_b) is obtained, using (2.14), from

$$\int_o^{T_b} V_t i_t\,dt \qquad (2.15)$$

and this may be optimized for a given pulse charge within the limits of a permissable energy spread and r-f power source by suitable choice of microwave parameters.

Equations (2.14) and (2.15) show preference for circuits with protracted fill times and high attenuation parameters, factors which are contrary therefore, to the steady state high current requirements for optimum efficiency at the lowest attenuation. Consequently, in providing a single system with reasonable steady state and stored energy capability the designer must seek a compromise and the use of alternate connection arrangements between the waveguides and the r-f power source can assist in this regard.

The above discussion disregards the transit time of the electron on the basis that $\beta_e \gg v_g/c$ and assumes that the electron bunches are located at the crest of the electric field. Furthermore, the beam pulse has been considered long enough (a minimum of several r-f cycles) such that the Fourier analysis of the induced finite wave train extends over a sufficiently limited range of wavelengths for superposition theory to remain valid.[2]

Space Charge and Transient Field Effects During Bunching

Two techniques for the capture and bunching of injected particles have been commonly adopted in the past in order to provide desirable bunch positioning and acceleration. One method utilizes a phase velocity of light circuit and arranges for electrons that enter the waveguide, during reversal of the electric field, to slip back to the crest of the wave after traversing a short distance and gaining sufficient energy to become synchronous. An alternate technique makes use of a tapered variable phase velocity structure (usually but not always less than c) that is arranged to accept particles which are injected at phase positions remote from the zero field position. This approach can offer a wide selection of bunching characteristics and asymptotic phase location by suitable choice of injection energy, and electric field and phase velocity variation over the first few wavelengths. One version suppresses phase oscillations[7] in bringing the particles together, even from phase positions behind the crest, and the laminar nature of the phase orbits offer advantages in beam focusing as well as reducing space charge forces during the critical "soft" period immediately after injection.

Typical S-band phase orbit plots for a $v_p = c$ and a variable v_p circuit are compared in Figures 3A and 3B respectively. The diagonal lines superimposed on the phase orbits represent intercepts of a time domain program which has been developed to provide bunch length and charge distribution information both in space and time. The time has been recorded in units of r-f cycle (ωt) normalized to the entry time of the first injected particle of interest. The cross-hatched contours represent charge distributions at specific times during the bunching process. Considering $\pm 30°$ uniform intensity injection, Figure 3A shows that early injection phases will cross later phase trajectories at points marked X, attempting to half the bunch length after traversing a short distance. This causes an intense build up of charge at the front of the bunch during a period when the particles are losing energy and are in a low electric field. For strongly confined beams of moderate intensity (1-2 amps) and small cross-section (2-3 mm), space charge fields can predominate (see inset Figure 3A) to cause instabilities which may be prevented by relaxation of the beam confinement. Injection over the same phase width but to one side of the zero phase position will, with this type of buncher, cause a rapid broadening of the emergent bunch.

On the other hand, considering 60° uniform

intensity injection, Figure 3B indicates an approach to adiabatic conditions where the initial charge distribution undergoes a gradual compression. The bunch rides well forward of the crest of an increasing velocity wave such that the shrinking bunch length (ℓ) and increasing beam energy (γ) compensate space charge forces and the beam is not too "stiff" to continue bunching. These conditions are suitable for high current operation within the limits of stability as determined by the relative amplitudes of the circuit and space charge fields across the bunch.

The space charge axial longitudinal electric field (E_s), transformed into the laboratory frame of reference, for a variety of charge distributions in a cylindrical bunch model has been included in Appendix I. Figure 4 shows the variation of the terminal space charge field with bunch geometry and energy in units of rest mass (γ). In general, this field decreases relatively slowly with increasing γ in the 100 to 500 Kev region and increases rapidly with reduction of bunch length (ℓ) and diameter (2a). Figure 5 shows the axial distribution of longitudinal field along the bunch for various charge distributions and (a/ℓ) ratios. The large field differential across the non-symmetrical triangular charge distribution, a situation not uncommon during short interaction periods in some bunch forming systems (Fig. 3A), should be noted.

The two simultaneous first order differential equations normally used for light beam loading conditions[7] and relating incremental energy gain and phase shift, can be modified by superimposing the space charge field (E_s) distribution upon the beam induced (E_{bz}) and applied circuit (E_{oz}) fields, and computed to first order by iterative step function solutions. Under steady state conditions, $o<z<\bar{v}_{gz}t$, and for symmetrical charge distributions, see Figure 4, we can write for the center of the bunch, δ_m, (measured from the field zero position),

$$\frac{d\gamma_{zm}}{dz}(.511) = -\bar{E}_z \sin\delta_m - \bar{E}_{bz} \qquad (3.1)$$

and

$$\frac{d\delta_m}{dz} = \frac{2\pi}{\lambda_o}\left(\frac{1}{\beta_w} - \frac{1}{\beta_{em}}\right) + \Delta\delta_r \qquad (3.2)$$

where $\gamma_{zm} = (1 - \beta_{em}^2)^{-1/2}$ and $\Delta\delta_r$ is the phase shift due to reactive distortion of the field which can be significant for heavy beam loading conditions. For a thin disc at the front of the bunch, δ_f,

$$\frac{d\gamma_{zf}}{dz}(.511) = -\bar{E}_z \sin\delta_f - \bar{E}_{bz} + \bar{E}_{sf} \qquad (3.3)$$

and

$$\frac{d\delta_f}{dz} = \frac{2\pi}{\lambda_o}\left(\frac{1}{\beta_w} - \frac{1}{\beta_{ef}}\right) + \Delta\delta_r \qquad (3.4)$$

and at the rear of the bunch, δ_b,

$$\frac{d\gamma_{zb}}{dz}(.511) = -\bar{E}_z \sin\delta_b - \bar{E}_{bz} - \bar{E}_{sb} \qquad (3.5)$$

and

$$\frac{d\delta_b}{dz} = \frac{2\pi}{\lambda_o}\left(\frac{1}{\beta_w} - \frac{1}{\beta_{eb}}\right) + \Delta\delta_r \qquad (3.6)$$

Simple considerations show that a limiting condition to avoid debunching for this symmetrical charge distribution case ($E_{sf} = E_{sb}$) will be,

$$\left(E_{sf} + E_{sb}\right) < -E_z\left(\sin\delta_b - \sin\delta_f\right) < 2E_z \cos\delta_m \sin\left(\frac{\pi\ell}{\lambda_g}\right) \qquad (3.7)$$

giving a relationship between space charge and circuit fields for a given bunch phase position and length. For example, from Figure 4, a bunch 5mm in diameter and 10mm long with a uniform charge distribution has an $E/Q = 3.5$ at 500 kv. For a phase location of $\delta_m = -60°$ in a buncher waveguide of $v_p = 0.85c$, equation (3.7) gives the relationship,

$E_z f/i > 20.3$ (f in KMc, i in amperes)

i.e. for 12 amps at S-band $E_z > 85$ kv/cm. This compares with 46 kv/cm for a symmetric triangular charge distribution.

By combining the space charge modified equations of motion with the transient electric field expression we can obtain phase orbital information for high current stored energy operation of the buncher. The time domain program offers a simple method of achieving transition from the steady state zone to the transient region by monitoring the power and induced field progression in accordance with the cavity group velocities and at any required time ($t=z/\bar{v}_{gz}$) during the short beam pulse the step by step computations can revert to the transient field equations.

Figure 6 shows phase orbit plots for high current short pulse operation. Under some circumstances the heavy beam loading condition can be advantageous causing slow bunching and phase slippage towards the zero field position in the steady state zone. Then, at appropriate short pulse lengths, the bunch will enter the transient region still low enough in energy to slip back towards the crest in the absence of the steady state beam loading field component, and continue bunching while extracting stored energy from the cavities. Some operational data relating to the S-band buncher in Figure 6B will be presented in a following section.

The above analysis assumes that a constant beam diameter is maintained throughout the bunching trajectory and no allowance is made for circuit shielding effects which appear low for $\ell << \lambda$ (neglecting passage through the disc apertures).

High Current Operation With a 10 Mev S-Band Linear Accelerator

Under the sponsorship of the Defense Atomic Support Agency (DASA) and the Boeing Company, a series of high current tests were conducted in December, 1963 and January, 1964, at Seattle on a three section S-band linear accelerator energized from a 16

MW peak r-f power system. The steady state performance characteristics of this machine for different modes of operation are shown in Figure 7. All three sections are of a non-uniform impedance design and the first half of the first section comprises a suppressed phase orbit oscillation, reduced phase velocity buncher. It was recognized that because the first two sections had been optimized for high steady state conversion efficiency (85%) the low fill times of approximately 230 ns per guide precluded the attainment of a high stored energy. Nevertheless, a total of 3.2 joules was available with 8 MW peak r-f power applied to each section and on the basis of 50% energy extraction, dependent upon the pulse duration it was expected that pulse currents an order of magnitude larger than the i_m value might be demonstrated. To meet this requirement a higher perveance diode gun was designed to replace the normal source and an additional thin lens (cross-over) assembly was added to the existing double lens and collimating system. A cathode emission rating of 20 amperes at 150 kv was chosen, and the location and size of the beam minimum was arranged to coincide with that of the original lower perveance geometry in order to satisfy the inflector and focusing requirements. Figure 8 shows the injection system in its normal configuration comprising a diode gun, two pairs of inflector plates, one of each pair being coaxially driven by a thyratron for independent fast start and stop control of the injected beam, tungsten collimators, a prebuncher cavity and focusing coils.

The tests demonstrated beam currents of up to 8 amperes for 30 nanoseconds (240 Ans) and with energy spectra consistent with the large extraction of stored energy.[13] A subsequent series of tests were conducted using a hybrid r-f power combiner to connect both arms of the klystron to the first waveguide section. Under these conditions, between 14 and 15 MW of r-f power produced accelerated pulses through the first section of up to 12 amperes (320 Ans - the limitation of the injection system). Average pulse energies ranged from 7 to 4 Mev for pulses with increasing levels of charge. Some typical wave forms taken during these tests and approximate pulse spectra, as computed from a succession of absorption measurements with increasing thicknesses of aluminum, are shown in Figure 9. When operating in the higher energy connection B, 160 Ans pulses at 2.7 amperes peak and 20 Mev is obtained. In general, the performance was in good agreement with the transient theory and confirmed that 50-60% of the stored energy could be extracted by the beam.

Conclusions

The conflicting high current requirements of low IL for steady state operation and high IL for stored energy, forces a compromise for those systems requiring both capabilities. It is clear that the use of lower frequencies enable higher fill time and stored energy to be achieved. Furthermore, the larger bunch dimensions will reduce space charge forces and for a given circuit electric field strength the phase stability limitations will be extended for a fixed ℓ/λ_g (equations (3.1)-(3.7).

A relationship between stored energy, electric field strength and frequency can be obtained by substituting for r-f peak power in the stored energy equation to give

$$U = E^2 L/\omega \qquad (r/Q)^{-1}$$

as r/Q is a constant of geometry virtually independent of frequency and $\bar{V} = \bar{E}L$, this indicates that the accelerated pulse charge

$$it \propto E^2/\omega \bar{E}$$

A crucial question yet to be resolved is the dependence (if any) of the breakdown value of electric field strength with frequency. However, if routinely achieved S-band field strengths of 200-250 kv/cm are conservatively reduced to 110 kv/cm and applied to a 425 Mc system, 160 joules could be stored in a two meter section with 20 MW input r-f power to produce a zero loading energy of 22 Mev. Considering only 25% energy extraction, to prevent excessive energy spread, this could produce a 100 ampere 20 ns beam pulse.

Preliminary studies indicate that short pulse currents in the 10-100 ampere range can be bunched and accelerated, the energy spread being directly related to the total pulse charge and stored energy. The energy spread, due to heavy extraction of stored energy, prevents efficient transportation of the beam to a target zone and results in considerable loss of current. It is suggested that a reduction of energy spread can be obtained by combining the inherent transient sweep of the bunch phase position with a ramped injection phase or gun voltage such that the bunch migrates towards the crest during the pulse to compensate for the depletion of stored energy.

A high fill time stored energy requirement ($T_f = 2ILQ/\omega$) can be satisfied by techniques other than reducing the frequency, such as the use of higher order modes. For example, Figure 10 compares a test cold stack of S-band higher order mode cavities with the standard variety. The narrower pass band characteristics of these much larger cavities provide high values of Q and T_f with an associated reduction in shunt impedance. This approach also offers some buncher design advantages in that phase velocity changes can be introduced over the existing relatively short trajectory distances between discs.

Ultimate high current short pulse performance has not been demonstrated to date owing to the inability of existing injection systems to provide limiting short pulse times and/or high peak currents. Well-defined beams of 200 amperes at 200-250 kv are commonly demonstrated in 20 MW r-f power tubes and higher intensities can be achieved with existing techniques using relatively large cathodes. The combination of high current and very short pulses however, is another matter. Short pulse operation concepts include:

(a) cathode and grid pulsing of small low capacitance, high emission buttons, (e.g. LaB_6 and YB_6 are capable of greater than 100 amperes/cm^2 emission),
(b) fast inflection and beam sweeping techniques,
(c) exploding replaceable cathodes,
(d) chopping and prebunching at low frequencies and subsequent pulse compression to produce individual rf burst,
(e) the possible future use of multiple high power laser beams focused through the gun envelope onto a small emitter, etc.

Beams of high perveance create grid and cathode life problems in case (a) as does short focal length for case (b), due to space charge broadened beam cross section (positive ion neutralization excepted) and magnetic confinement requirements.

In general, sub-nanosecond operation suggests the use of microwave devices and as an example, Fig. 11A shows two higher order mode transverse magnetic chopper cavities orthogonally arranged and phased in quadrature to produce rotation of a 120 kv electron beam. Operation of a similar chopper cavity located at the gun anode produces sub r-f cycle beam lengths which after traversal through the dual cavity system can be viewed on a tungsten screen. The circular pattern of the non-chopped d-c beam shown in Fig. 11 (1B) reduces to Fig. 11 (2B), when the gun chopper sweeps the beam symmetrically across a centrally located clipping aperture, showing two arc lengths equivalent to 90° bunches. With offset or biased chopping Figures 11 (3B) and (4B) indicate single bunch chopping down to 40°, i.e. 4×10^{-11} sec. These tests were conducted with a 3 ampere beam at S-band frequencies but suggest that lower frequency chopper cavities, rapidly discharged by trigger or multipactor devices, may provide a means for obtaining short pulse high current performance. Rotation of the high power beam would also alleviate a serious collector problem during the "beam off" condition.

In the limit, full exploitation of the stored energy regime will be contingent on resolving several questions of a fundamental nature such as, the mechanism of energy transfer from fields in the central region of a cavity to a single r-f bunch of massive charge content and, the effect this has on the extended transient pulse containing several following bunches.

Appendix I

Space Charge Axial Longitudinal Electric Field in the Laboratory Frame for Uniform Radial and Variable and Uniform Linear Charge Distributions in a Cylindrical Electron Bunch Model in the Proper Frame

Consider a cylindrical electron bunch in the proper frame with an over all length ℓ' and diameter 2a. Assume the total contained charge, Q, is distributed uniformly in the radial direction and with a linear charge density distribution $\rho_{z'}$ indicated by (a), (b) and (c) in Figure 12. We wish to determine the magnitude and direction of the longitudinal electric field (E_s) at any point along the axis of the bunch and for the following terminal cases:

Case (a) Forward peak triangular charge distribution, (E_s) at $z=+\ell/2$.
(b) Uniform charge distribution, (E_s) at $z = \pm \ell/2$.
(c) Central peak triangular charge distribution, (E_s) at $z = \pm \ell/2$.
(d) Forward peak triangular charge distribution (E_s) at $z = -\ell/2$.

Case (a) Forward Peak Triangular Charge Distribution. (E_s at $z = \ell/2$).

Assuming a small volume at point q from Gauss' law the electric field at the point UL' may be written:

$$E_{s'} = \int_V \rho_{z'}\, dz'rdrd\phi/4\pi\epsilon_o R'^2 \qquad (4.1)$$

and over any volume of interest between the upper limit (UL') and the lower limit (LL') the following substitutions can be made:

$$R' = \left[r + (UL' - z')^2\right]^{1/2}$$

and

$$\rho_{z'} = \rho_o\left(1/2 + z'/\ell'\right)$$

where $\rho_o = 2Q/\pi a^2\ell'$
to give

$$E_{s'} = \frac{Q}{\pi\epsilon_o a^2 \ell'}\int_{LL'}^{UL'}\left(\frac{1}{2}+\frac{z'}{\ell'}\right)dz'\int_o^a \frac{(UL'-z')rdr}{\left[r^2+(UL'-z')^2\right]^{3/2}} \qquad (4.2)$$

Considering the terminal electric field at $z'=\ell'/2$ by integrating over the limits $UL'=\ell'/2$, $LL'=-\ell'/2$, and transforming into the laboratory frame we obtain,

$$\frac{E_s}{Q} = \frac{1}{2\pi\epsilon_o a^2}\left[1+2\left(\frac{a}{\gamma\ell}\right)-\sqrt{1+\left(\frac{a}{\gamma\ell}\right)^2}-\left(\frac{a}{\gamma\ell}\right)^2 \ln\frac{1+\sqrt{1+\left(\frac{a}{\gamma\ell}\right)^2}}{\left(\frac{a}{\gamma\ell}\right)}\right] \qquad (4.3)$$

for an electron velocity $\beta_e c$ such that the total electron energy in units of rest mass

$$\gamma = \left[1 - \beta_e^2\right]^{-1/2}$$

and where the constant ϵ_o and Q, the total charge, are Lorentz invariants. (The radial dimension "a" also transforms directly when measured perpendicular to the velocity vector.)

Case (b) Uniform Charge Distribution

In this case $\rho_{z'} = Q/\pi a^2\ell'$ and equation (4.1) reduces to

$$E_{s'} = \frac{Q}{2\pi\epsilon_o a^2 \ell'}\left[\sqrt{a^2 + (UL'-z')^2} + z'\right]_{LL'}^{UL'} \qquad (4.4)$$

which after transformation gives the axial terminal electric field as

$$\frac{E_s}{Q} = \frac{1}{2\pi\epsilon_o a^2}\left[1 + \left(\frac{a}{\gamma\ell}\right) - \sqrt{1 + \left(\frac{a}{\gamma\ell}\right)^2}\right] \qquad (4.5)$$

Case (c) Central Peak Triangular Charge Distribution

Substituting in equation (4.1),

$$\rho_{z'} = (2\rho_o/\ell')(\ell'/2 \mp z') \qquad \text{when } z' \gtrless 0$$

where $\rho_o = 2Q/\pi a^2 \ell'$ and dividing the integration into two parts about the mid-plane ($z' = 0$) we obtain

$$E_{s'} = \frac{2Q}{\pi\epsilon_o a^2 \ell'^2}\left[\left(\frac{\ell' z'}{2} + \frac{z'^2}{2} + K'\left(\frac{\ell'}{2} + z'\right) + \frac{1}{2}\left[(UL' - z')K' + a^2 \ln(UL' - z' + K')\right]\right)_{LL'}^{0} + \left(\frac{\ell' z'}{2} - \frac{z'^2}{2} + K'\left(\frac{\ell'}{2} - z'\right) - \frac{1}{2}\left[(UL' - z')K' + a^2 \ln(UL' - z' + K')\right]\right)_{0}^{UL'}\right] \qquad (4.6)$$

where

$$K' = \sqrt{a^2 + (UL' - z')^2}$$

The terminal axial electric field after transformation is then given by

$$\frac{E_s}{Q} = \frac{2}{\pi\epsilon_o a^2 (\gamma\ell)^2}\left[\frac{\gamma\ell}{2}\left(\sqrt{a^2 + \left(\frac{\gamma\ell}{2}\right)^2} - \sqrt{a^2 + (\gamma\ell)^2} + \frac{\gamma\ell}{2}\right) - \frac{a^2}{2}\left(\ln a - 2\ln\left[\frac{\gamma\ell}{2} + \sqrt{a^2 + \left(\frac{\gamma\ell}{2}\right)^2}\right] + \ln\left[\gamma\ell + \sqrt{a^2 + (\gamma\ell)^2}\right]\right)\right] \qquad (4.7)$$

Case (d) Forward Peak Triangular Charge Distribution (E_s at $z = -\ell/2$)

This case determines the axial electric field extending from the opposite end of the charge configuration treated in case (a). Now we have

$$R' = \sqrt{r^2 + (z' - LL')^2}$$

and the $\rho_{z'}$ distribution remains unchanged to give the the following expression in the laboratory frame of reference.

$$\frac{E_s}{Q} = \frac{1}{2\pi\epsilon_o a^2}\left[1 - \sqrt{1 + \left(\frac{a}{\gamma\ell}\right)^2} + \left(\frac{a}{\gamma\ell}\right)^2 \ln\left(\frac{1 + \sqrt{1 + \left(\frac{a}{\gamma\ell}\right)^2}}{\left(\frac{a}{\gamma\ell}\right)}\right)\right] \qquad (4.8)$$

Substituting appropriate values for UL' and LL' in the above cases enables the electric field distribution within the bunches to be computed, some examples of which have been shown in Figure 5.

Units

The terminal electric field values at $r = 0$ obtained from the equations (4.3), (4.5), (4.7) and (4.8) have been plotted in Figure 4 and 5 using the MKS system of units. The results have been multipled by 10^{-14} to present the data in terms of kv/cm/nano-coulomb, and may be reduced to electric field in kv/cm for a given r-f frequency (f) measured in KMc and a current (i) in amperes, averaged over the r-f cycle, as follows:

$$E_s = (E_s/Q)\ (i/f)\ \text{kv/cm}. \qquad (4.9)$$

In general, electron bunch model computations for oblate and prolate spheriods of elliptic profile are not significantly different to the data presented on the accompanying graphs for cylindrical bunch models.

Acknowledgements

The author wishes to express his gratitude to Miss B. Mecklenburg for her valuable assistance in compiling enumerable computer programs over the past few years.

References

1. E. L. Chu and W. W. Hansen, J. App. Phys. 18, 996 (1947)
2. J. C. Slater, Revs. Mod. Phys. 20, 473 (1948)
3. M. Chodorow, et al., Rev. Sci. Inst., Vol. 26, 134 (1955)
4. H. Leboutet, Annales de Radioélectricite XIII, No. 52, (1958)
5. R. B. Neal, J. App. Phys. 29, 1019 (1958)
6. R. B. Neal, Report No. ML513, Microwave Lab., Stanford University (1958)
7. J. Haimson, IRE Trans. Nucl. Sci 9, 32 (1962)
8. M. G. Kelliher and R. Beadle, Nature 187, 1099 (1960)
9. M. C. Crowley-Milling et al., Nature 191, 483 (1961)
10. G. Saxon et al., I.E.E.E. Proc. 110, 1365 (1963)
11. P. Wilson, High Energy Physics Lab Report No. HEPL-297, Stanford University (1963)
12. G. A. Loew, Report No. ML740, Microwave Lab., Stanford University (1960)
13. J. Haimson and N. Pering, Defense Atomic Support Agency, Report No. DASA 1523 (1964)

TABLE I

PULSE SHORTENING DATA FOR KLYSTRON DRIVEN LINEAR ACCELERATORS

Test Date	Machine Designation	No Load Energy (Mev)	Total Input Peak r-f Power (Mw)	Number of Sections	Rated Beam Pulse Length (μsec)	PEAK CURRENT (ma)			Percent $\left(\frac{i_s}{i_m}\right)$	Remarks
						Rated Value (i_r)	Start of Pulse Shortening at Rated Beam Pulse Length (i_s)	Value For Maximum Conversion Efficiency (i_m)		
June 1958	Livermore	27	10	2	1.9	250	270	640	42.2	$\frac{\pi}{2}$ mode
Feb 1960	Danish									$\frac{\pi}{2}$ mode
		15	5	1 + 1	4.5	100	325	350	93	Sections connected in series
		12.5	5	2	4.5	260	315	650	48.5	2.5 Mw per section
		8.5	5	1	4.5	450	650	770	84.5	One section only
Nov 1961	Darmstadt	61	14	2	2.1	120	180	225	80	$\frac{2\pi}{3}$ mode
Feb 1962	Q.M.C.	32	20	4	5.0	450	650	940	69	$\frac{\pi}{2}$ and $\frac{2\pi}{3}$ modes
Oct 1962	Hill AFB	35	14.5	2	2.7	350	740 Maximum injection. No pulse shortening observed.	595	> 124	$\frac{2\pi}{3}$ mode (variable impedance) No pulse shortening observed up to the limits of injection and pulse line length.
July 1963	Boeing Connection A	16	16	2	8.0	1000	> 2700 Maximum injection. No pulse shortening observed.	1600	> 170	$\frac{2\pi}{3}$ mode (variable impedance) No pulse shortening observed up to the limits of injection and pulse line length.

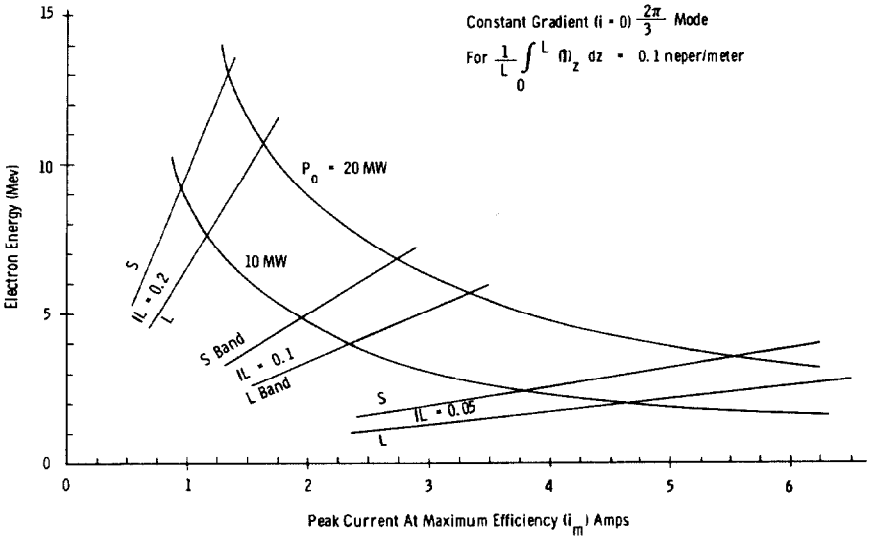

Fig. 1. Beam Energy Versus i_m for Steady State Operation with Low Attenuation Waveguides.

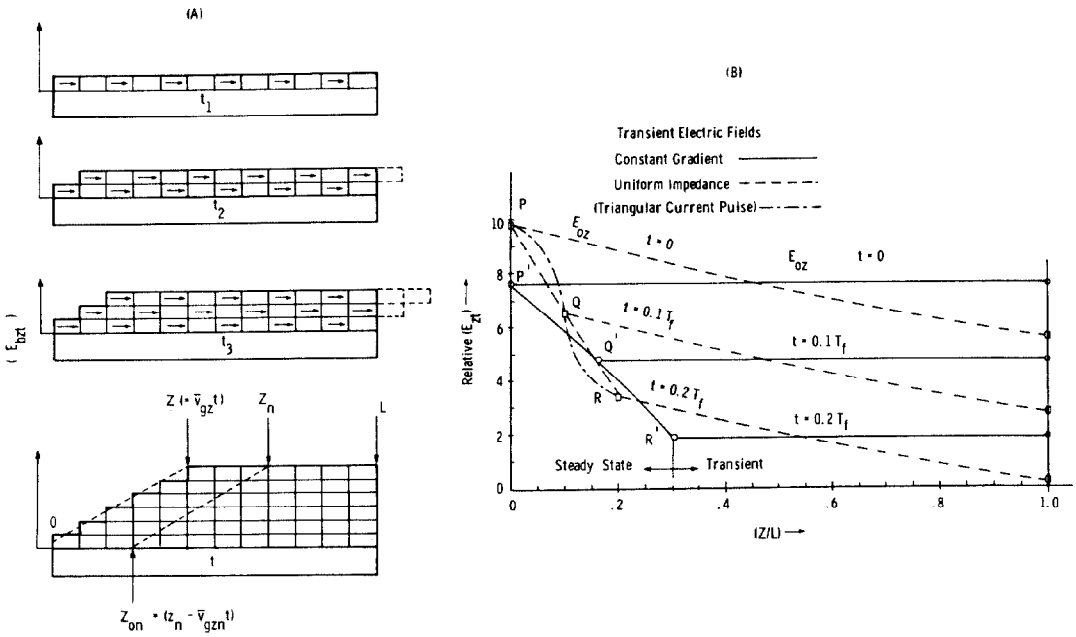

Fig. 2. Beam Induced Field Growth and Transient Electric Field Patterns.

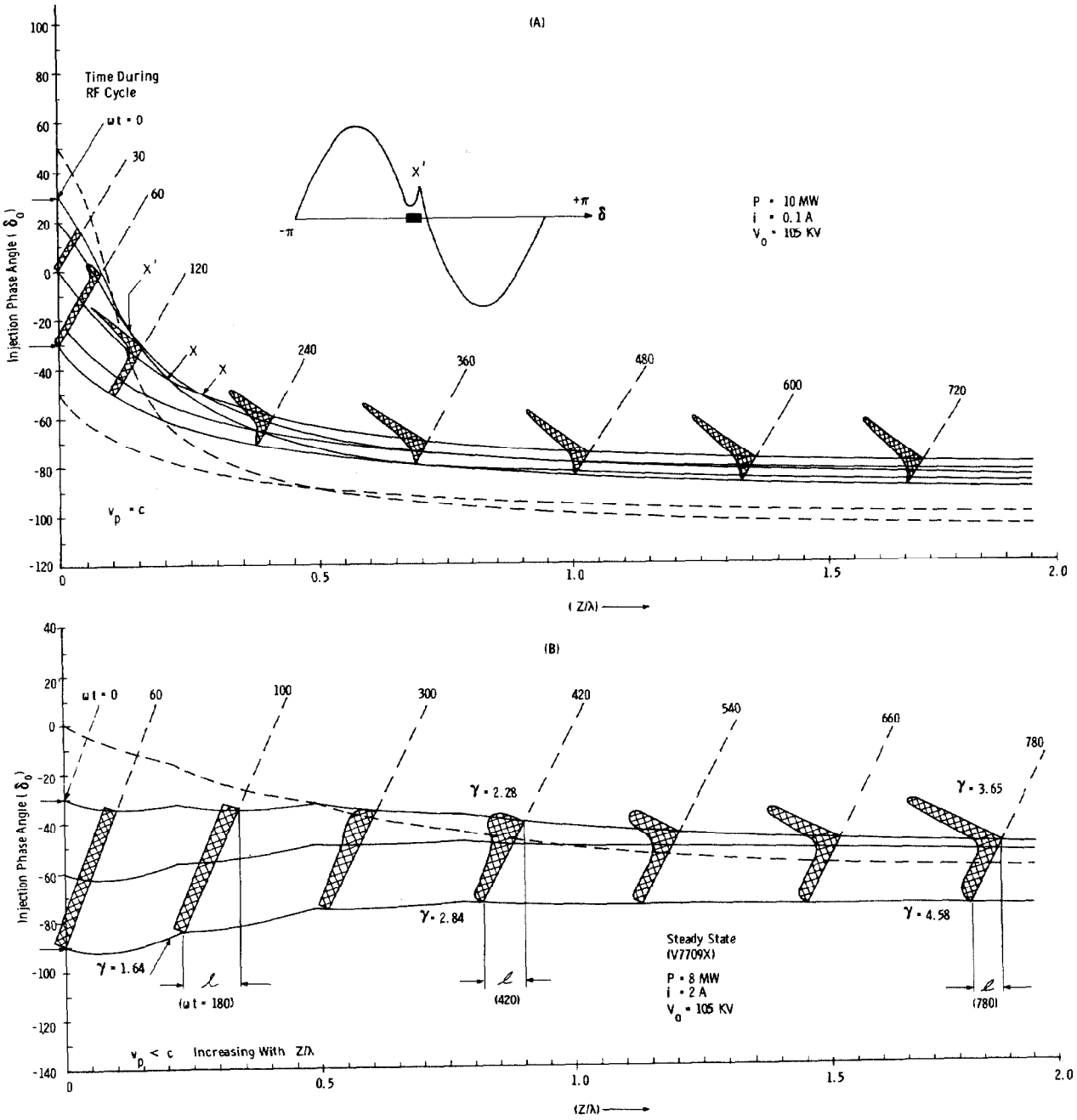

Fig. 3. Electron Phase Orbit Plots for $v_p = c$ and Variable v_p Circuits.

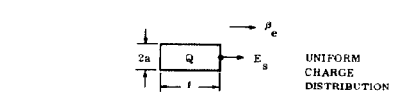

$$\frac{E_s}{Q} = \frac{10^{-14}}{2\pi\epsilon_o a^2}\left[1 + \left(\frac{a}{\gamma\ell}\right) - \sqrt{1 + \left(\frac{a}{\gamma\ell}\right)^2}\right] \text{ kv/cm/nanocoulomb}$$

("a" and "f" in meters)

$$\gamma = \left(\frac{V}{511} + 1\right)$$

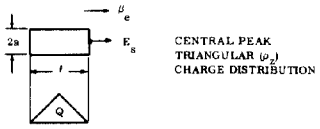

$$\frac{E_s}{Q} = \frac{2 \times 10^{-14}}{\pi\epsilon_o a^2 (\gamma\ell)^2}\left[\frac{\gamma\ell}{2}\left\{\sqrt{a^2 + \left(\frac{\gamma\ell}{2}\right)^2} - \sqrt{a^2 + (\gamma\ell)^2} + \frac{\gamma\ell}{2}\right\}\right.$$

$$\left. - \frac{a^2}{2}\left\{\ln a - 2\ln\left(\frac{\gamma\ell}{2} + \sqrt{a^2 + \left(\frac{\gamma\ell}{2}\right)^2}\right) + \ln\left(\gamma\ell + \sqrt{a^2 + (\gamma\ell)^2}\right)\right\}\right] \text{ kv/cm/nanocoulomb}$$

("a" and "f" in meters)

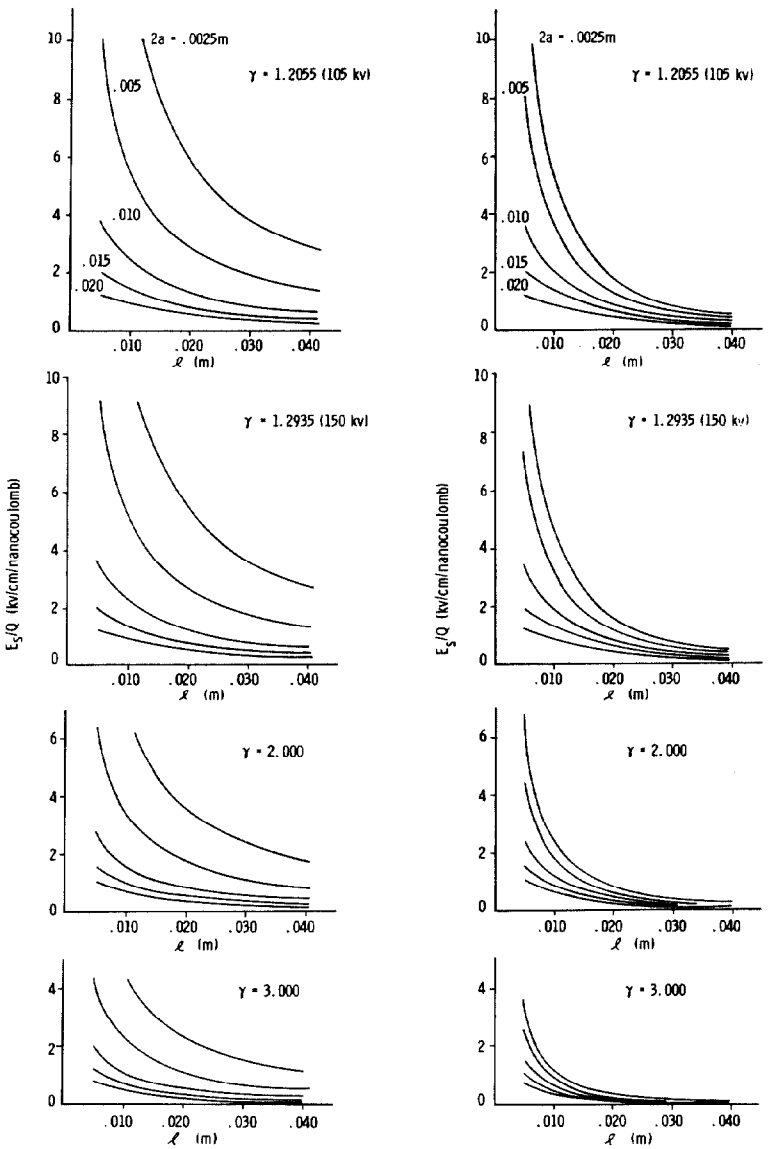

Fig. 4. Space Charge Axial Longitudinal Terminal Electric Field for a Cylindrical Bunch Model.

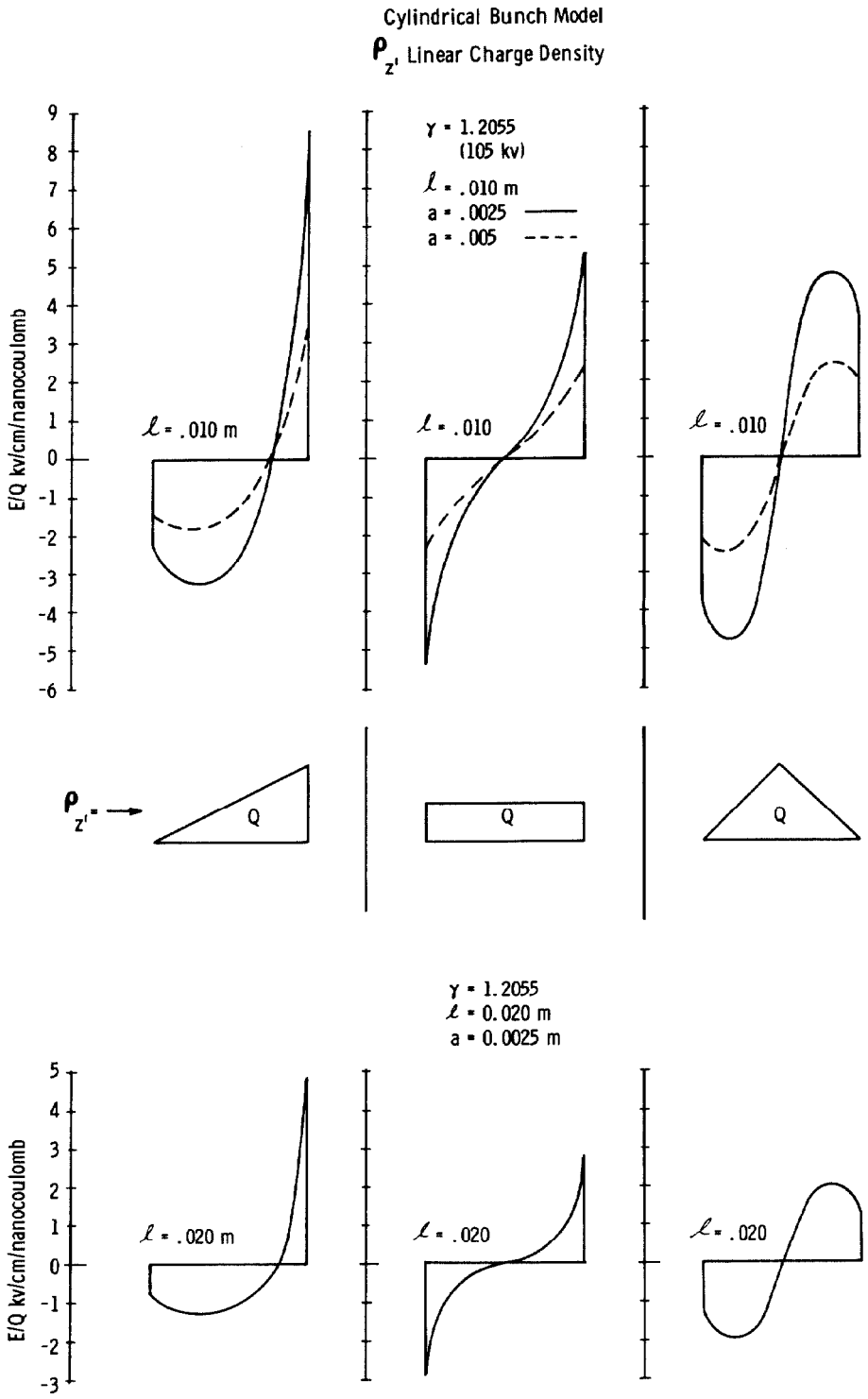

Fig. 5. Space Charge Longitudinal Electric Field Axial Distribution for Various Charge Distributions in a Cylindrical Bunch Model.

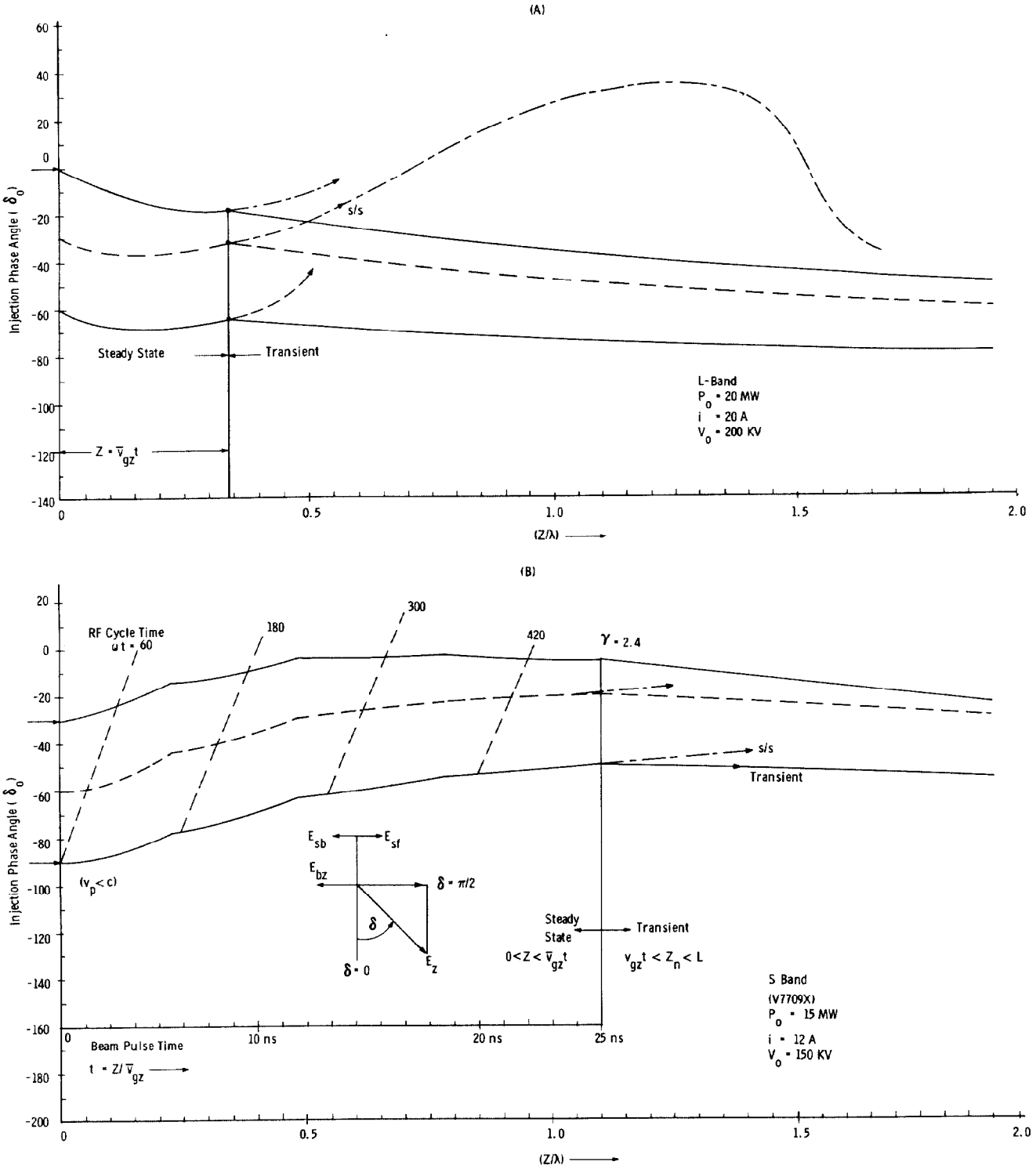

Fig. 6. High Current Electron Phase Orbit Plots Showing Transient Region.

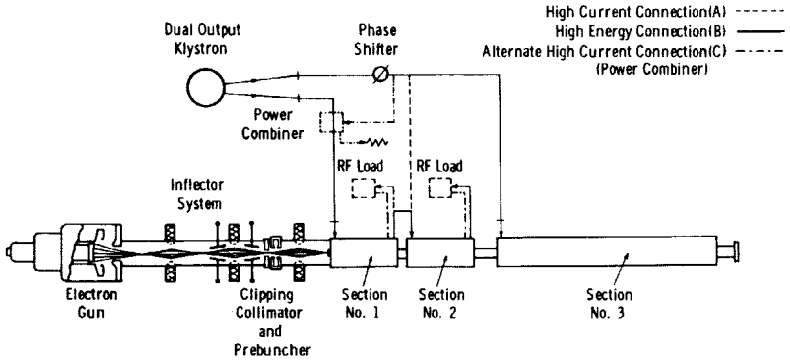

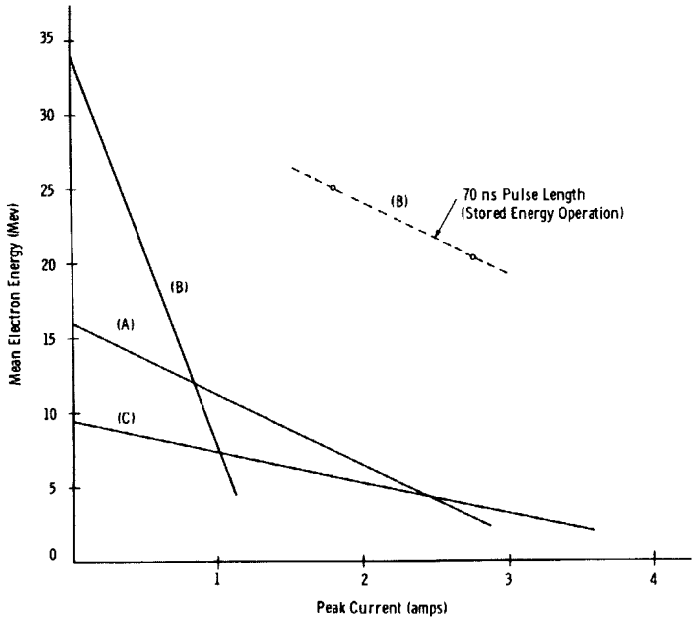

Fig. 7. Steady State Performance Characteristics of a 3 Section S-Band Linear Accelerator.

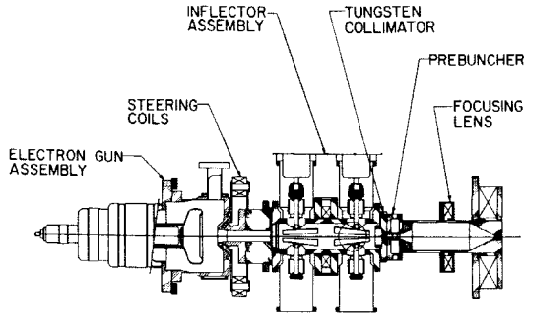

Fig. 8. Injection System for Short Pulse and Prebuncher Operation.

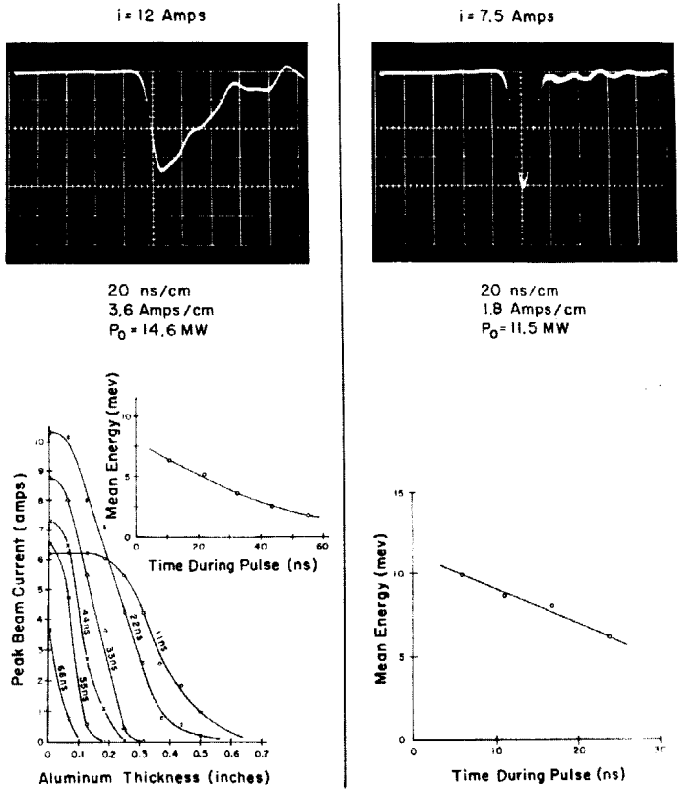

Fig. 9. Beam Spectra and Waveforms for High Current Stored Energy Operation.

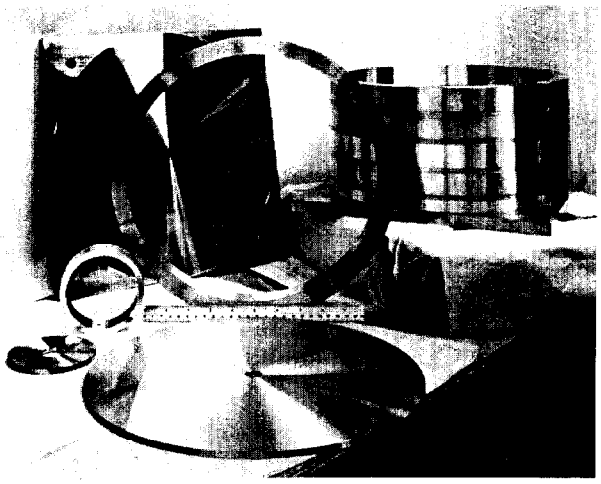

Fig. 10. Comparison of Standard and Higher Order Mode S-Band Cavities.

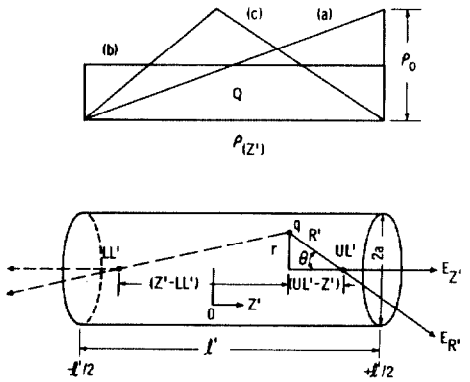

Fig. 12. Cylindrical Bunch Model Co-ordinates.

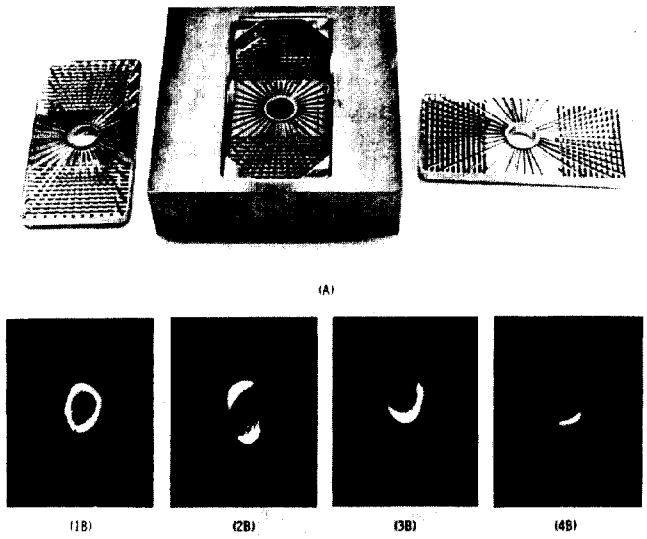

Fig. 11(A). Transverse Magnetic Higher Order Mode Dual Cavity Assembly for Monitoring Bunch Length.

Fig. 11(B). Beam Rotation and RF Chopping at S-Band Frequency.